

Influence of the electron spin resonance saturation on the power sensitivity of cryogenic sapphire resonators

Vincent Giordano, Serge Grop, Pierre-Yves Bourgeois, Yann Kersalé, and Enrico Rubiola

Citation: [Journal of Applied Physics](#) **116**, 054901 (2014); doi: 10.1063/1.4891685

View online: <http://dx.doi.org/10.1063/1.4891685>

View Table of Contents: <http://scitation.aip.org/content/aip/journal/jap/116/5?ver=pdfcov>

Published by the [AIP Publishing](#)

Articles you may be interested in

[Resonator power to frequency conversion in a cryogenic sapphire oscillator](#)

Appl. Phys. Lett. **103**, 043502 (2013); 10.1063/1.4816284

[Electromagnetic properties of sapphire, ruby, and irradiated ruby at frequencies of 30–40 GHz](#)

Appl. Phys. Lett. **99**, 102901 (2011); 10.1063/1.3635787

[Note: High sensitivity pulsed electron spin resonance spectroscopy with induction detection](#)

Rev. Sci. Instrum. **82**, 076105 (2011); 10.1063/1.3611003

[High Q -factor sapphire whispering gallery mode microwave resonator at single photon energies and millikelvin temperatures](#)

Appl. Phys. Lett. **98**, 222903 (2011); 10.1063/1.3595942

[Maser oscillation in a whispering-gallery-mode microwave resonator](#)

Appl. Phys. Lett. **87**, 224104 (2005); 10.1063/1.2137452



AIP | Journal of Applied Physics

Journal of Applied Physics is pleased to announce **André Anders** as its new Editor-in-Chief

Influence of the electron spin resonance saturation on the power sensitivity of cryogenic sapphire resonators

Vincent Giordano,^{a)} Serge Grop, Pierre-Yves Bourgeois, Yann Kersalé, and Enrico Rubiola
 FEMTO-ST Institute—UMR 6174, CNRS/ENSMM/UFCA/UTBM, 26 Chemin de l'Épitaphe, 25000 Besançon, France

(Received 10 June 2014; accepted 18 July 2014; published online 1 August 2014)

Here, we study the paramagnetic ions behavior in presence of a strong microwave electromagnetic field sustained inside a cryogenic sapphire whispering gallery mode resonator. The high frequency measurement resolution that can be now achieved by comparing two Cryogenic Sapphire Oscillators (CSOs) permit to observe clearly the non-linearity of the resonator power sensitivity. These observations that, in turn, allow us to optimize the CSO operation are well explained by the electron spin resonance saturation of the paramagnetic impurities contained in the sapphire crystal.
 © 2014 AIP Publishing LLC. [<http://dx.doi.org/10.1063/1.4891685>]

I. INTRODUCTION

Sapphire single crystal is a key material for numbers of very demanding scientific and technological applications. Even in its purest form, the sapphire single crystal always contains some paramagnetic impurities, which come from the raw material or are results of contamination during the growth process.^{1,2} Despite their low concentration, these accidental dopants turn out to be very useful in some innovative systems intended for high resolution measurements. The Cryogenic Sapphire Oscillator (CSO) incorporating a cryogenic sapphire whispering gallery mode resonator is currently the most stable frequency source. It achieves in an autonomous and reliable version a relative frequency stability better than 1×10^{-15} for integration times $\tau \leq 10\,000$ s, with at long term a frequency drift of 2×10^{-15} /day.^{3,4} The thermal compensation induced by the accidental paramagnetic impurities that substitute to Al^{3+} is essential for the achievement of the highest frequency stability.^{5,6} A high Q-factor microwave cryogenic resonator containing a small amount of Fe^{3+} can also be used as the amplifying medium to design a zero-field solid-state 12 GHz Maser^{7,8} or as the non-linear element for microwave third harmonic generation.^{9,10} Paramagnetic impurities in sapphire are also good candidates for the realization of quantum electrodynamics measurements.¹¹

In this paper, we study the behavior of paramagnetic dopants diluted in a sapphire high-Q microwave resonator in which a strong electromagnetic field is sustained. The Van-Vleck model is applied to calculate the dc-magnetic susceptibility induced at low power by the different paramagnetic species that can be found in the high quality sapphire crystal. The interaction between the paramagnetic dopants and the RF electromagnetic field is described through the classical two-levels Bloch equations. We show how the saturation of the Electron Spin Resonances (ESR) leads to a non-linear power sensitivity of the resonator frequency. Eventually, the stabilisation of the injected power to the resonator turnover

point allows us to optimise the oscillator frequency stability, which reaches a flicker floor of 3×10^{-16} extending until 10 000 s.

II. PARAMAGNETIC IONS DESCRIPTION

A. Standard magnetic susceptibility model

The presence of paramagnetic dopants in the crystal matrix and its impact on the propagation of an electromagnetic wave at the frequency ν are accounted for through the magnetic susceptibility $\chi(\nu) = \chi'(\nu) + j\chi''(\nu)$. χ' and χ'' represent, respectively, the phase shift and the power absorption induced by the ESR.¹² Let us assume that the sapphire crystal contains a density N of a paramagnetic ion presenting in its ground state two energy levels $|m\rangle$ and $|n\rangle$ separated by the ion ESR frequency ν_{mn} . Solving the Bloch equations for such a two level system interacting with the wave at the frequency ν leads for the real part of the susceptibility to a dispersive Lorentzian function that nulls at ν_{mn} :¹³

$$\chi'(\nu) = \chi_0 \frac{(2\pi\tau_2)^2 (\nu - \nu_{mn})\nu_{mn}}{1 + (2\pi\tau_2)^2 (\nu - \nu_{mn})^2 + \Omega^2 \tau_1 \tau_2}, \quad (1)$$

where τ_1 and τ_2 are the ion spin-lattice and spin-spin relaxation times, respectively. Ω is the Rabi frequency and χ_0 is the dc-susceptibility. Similarly, we found an absorption Lorentzian lineshape for $\chi''(\nu)$, whose linewidth at low power is $\Delta\nu_{mn} = 1/\pi\tau_2$.

Ω is proportional to the ESR transition probability σ_{mn} and to the RF magnetic field B_{RF}

$$\Omega = \frac{g\mu_B B_{RF}}{\hbar} \sigma_{mn}, \quad (2)$$

where g is the Landé factor, μ_B the Bohr Magneton, and \hbar the reduced Planck constant. The term $\Omega^2 \tau_1 \tau_2$ in the denominator of Eq. (1) is the saturation parameter proportional to the electromagnetic power felt by the ions. This term is generally neglected in the analysis of the paramagnetic ion behavior in the CSO sapphire resonator. However, as we will

^{a)}Electronic mail: giordano@femto-st.fr

see later, when the electromagnetic wave is confined in a high-Q factor cryogenic sapphire resonator, the saturation of the ESR can no longer be neglected.

The dc-susceptibility χ_0 results from the distribution of the ions on their energy levels through the effect of the thermal agitation. The derivation of χ_0 at a given absolute temperature T is straightforward by assuming (i) the energy separation between the ion ground state and excited state is large compared to $k_B T$, (ii) the ion orbital momentum is totally quenched by the crystal field, and thus, the ion in the crystal lattice behaves like a free spin S . With these assumptions, χ_0 follows the Curie law:¹⁴

$$\chi_0^C = \mu_0 N \frac{g^2 \mu_B^2}{3k_B T} S(S+1), \quad (3)$$

where μ_0 is the permeability of free space and k_B the Boltzmann constant.

B. On the validity of the ESR description

The Curie law has been derived for a free system of spin S , which consists in $2S+1$ levels equally spaced. Departures from the Curie law are well known for Sm^{3+} and Eu^{3+} as for these two rare-earth ions the first excited multiplet populations can not be neglected. Even for less exotic ions, in a real crystal, the ground state is splitted by the crystal field in multiple degenerated Kramer's doublets separated by a Zero Field Splitting (ZFS).¹⁵ The Table I gives the characteristics of the dominant paramagnetic species that can be found in high purity sapphire crystals.

Strictly speaking, for these ions, the dc-susceptibility should be calculated by using the Van Vleck equation²⁰

$$\chi_0^{VV} = \mu_0 N \frac{\sum_m (E_m^{(1)^2} - 2E_m^{(2)}) \exp(-E_m^{(0)}/k_B T)}{\sum_m \exp(-E_m^{(0)}/k_B T)}, \quad (4)$$

provided we know a Taylor expansion as a function of the applied magnetic field B_0 of each populated energy levels, i.e., $E_m = E_m^{(0)} + E_m^{(1)} B_0 + E_m^{(2)} B_0^2 + \mathcal{O}^3$. In a number of situations, the cumbersome calculation of the Van Vleck coefficients $E_m^{(k)}$ is avoided, and the dc-susceptibility is assumed to follow the Curie law. However, the current measurement resolution is such as it is necessary to know the degree of validity of this assumption. In Ref. 21, Boča uses the spin-hamiltonian formalism to derive the Van Vleck coefficients, and thus the dc-susceptibility expression for various systems

TABLE I. ESR of the Iron-group paramagnetic ions that can be found in high-purity sapphire crystals.

Ion	S	Ground state transitions	ν_{mn} (GHz)	σ_{mn}	τ_1 (ms)	τ_2 (ns)	Reference
Cr^{3+}	3/2	$ \frac{1}{2}\rangle \rightarrow \frac{3}{2}\rangle$	11.4	1.00	200	7	12 and 16
Mo^{3+}	3/2	$ \frac{1}{2}\rangle \rightarrow \frac{3}{2}\rangle$	165.0	2.00	0.1	12	17 and 18
Fe^{3+}	5/2	$ \frac{1}{2}\rangle \rightarrow \frac{3}{2}\rangle$	12.0	2.00	10	20	2 and 19
		$ \frac{3}{2}\rangle \rightarrow \frac{5}{2}\rangle$	19.3	1.25			
		$ \frac{1}{2}\rangle \rightarrow \frac{5}{2}\rangle$	31.3	0.0024			

presenting a ZFS. From his results, we calculated χ_0^{VV} for Cr^{3+} , Fe^{3+} , and Mo^{3+} in Al_2O_3 neglecting the rhombic zero-field splitting parameter. Figure 1 shows the comparison between the Curie Law and the Van Vleck model.

In the range of temperatures reachable with a modern two-stages cryocooler (3–10 K), the difference in the two dc-susceptibility values is less than 20%.

A second issue in the standard model arises from the case of Fe^{3+} ion. Eq. (1) is valid for a two levels system. Fe^{3+} has a spin $S=5/2$, and thus, its ground state is splitted in three Kramer's doublets: $|1/2\rangle$, $|3/2\rangle$, and $|5/2\rangle$. In the absence of a static magnetic field, there are, thus, three ESRs at the frequencies 12.0 GHz, 19.3 GHz, and 31.3 GHz. When dealing with a low power, the level populations stay almost those imposed by the thermal agitation. The susceptibility thermal behavior will be, thus, well represented by the Van Vleck model. At a high power, the differential saturation of these three transitions makes complex the derivation of the equations. The $|1/2\rangle \rightarrow |5/2\rangle$ transition at 31.3 GHz is only allowed owing the state-mixing induced by the crystal field. For a frequency ν near 10 GHz, it is thus justified to neglect this transition when calculating the evolution of overall magnetic susceptibility. About one third of the Fe^{3+} ion population is on the $|5/2\rangle$ level and is not affected by the RF magnetic field. We can reasonably conclude that the two levels model will lead to an overestimation of the impact of the ESR saturation on the magnetic susceptibility. We did not go further in the description of the Fe^{3+} ion behavior as the current uncertainties in the impurities concentration and in the ions relaxation times τ_1 and τ_2 make illusive a better quantitative analysis.

III. WHISPERING GALLERY MODE RESONATOR: LOW POWER OPERATION

Due to its high-Q factor at low temperature, the sapphire whispering gallery mode resonator constitutes a powerful tool to observe the behavior of the paramagnetic ions diluted in the crystal. The typical resonator geometry is shown in Figure 2.

For an operation in X-band, the sapphire cylinder has a diameter $30 \leq 2R \leq 55$ mm and a thickness $20 \leq H \leq 30$ mm. Its axis is parallel to the crystal C-axis within ± 0.5 degree. The resonator is placed in the center of a cylindrical gold

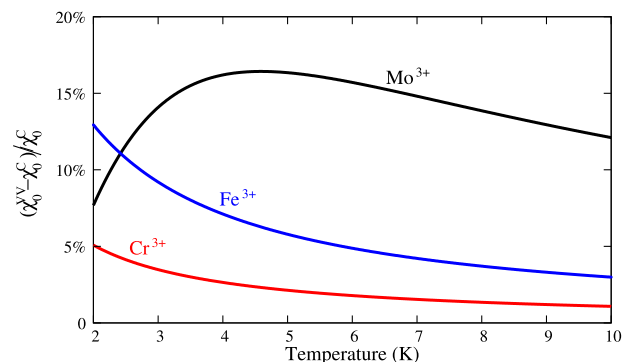


FIG. 1 Comparison between the Curie and the Van Vleck laws: $(\chi_0^{VV} - \chi_0^C)/\chi_0^C$ for Cr^{3+} (red), Fe^{3+} (blue), and Mo^{3+} (black) in Al_2O_3 .

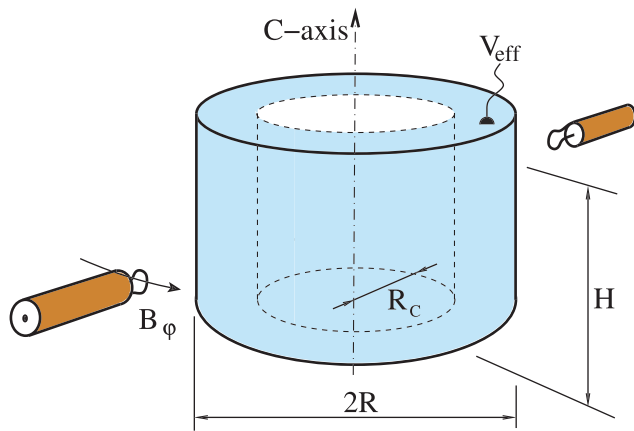


FIG. 2. The microwave whispering gallery mode resonator.

plated copper cavity and can be easily cooled down to about 3 K inside a two-stages cryocooler developing a power of 0.5 W at 4 K. Two diametrically opposed small magnetic loops excite the electromagnetic resonance modes of the structure. Among them, the high order hybrid modes called whispering gallery modes are characterized by a high degree of confinement of the electromagnetic fields inside the dielectric medium. In that case, the resonator quality factor is only limited by the sapphire dielectric losses which are very low at a cryogenic temperature.²² For a 10 GHz resonance mode, the typical unloaded Q-factor is 1×10^9 at 6 K. For a whispering gallery mode, the energy density is confined between the cylindrical dielectric–air boundary and the inner caustic surface $\rho = R_C$ (see Fig. 2). Elsewhere, the waves are evanescent. The resonator can, thus, be seen like a bent waveguide forming a ring.²³ The volume of this ring is $V_{eff} = \pi H(R^2 - R_C^2)$. In the configuration shown in Figure 2, the magnetic field generated by the loops is perpendicular to the cylindrical axis allowing to excite the quasi-transverse magnetic whispering gallery modes such as $WGH_{m,n,l}$ mode. The three integers m , n and l represent the electromagnetic field components variations along the azimuthal ϕ , radial ρ , and axial z directions, respectively.²⁴ We consider only the resonant modes with low radial and axial variations, i.e., those corresponding to $n = l = 0$ as they present the more efficient confinement inside the dielectric medium.

At low power, the temperature dependence of a given mode frequency ν is⁵

$$\frac{\nu(T) - \nu_0}{\nu_0} = AT^4 - \eta \frac{\chi'(\nu, T)}{2}. \quad (5)$$

ν_0 would be the mode frequency for a negligible circulating power, at $T = 0$ K and in the absence of any paramagnetic dopant. $A \approx -3 \times 10^{-12} \text{ K}^{-4}$ (Ref. 6) combines the temperature dependence of the dielectric constant and the thermal dilatation of the sapphire. The filling factor $\eta \approx 1$ for a high order whispering gallery mode. χ' is the real part of the ac susceptibility for a RF magnetic field perpendicular to the crystal C-axis. It is the sum of the contributions of all ion species contained into the crystal. The low power assumption means that the thermal distribution of the population on the energy levels of the paramagnetic impurities is not modified

by the RF magnetic field, i.e., $\Omega^2 \tau_1 \tau_2 \ll 1$. For a mode frequency below the ESR of the dominant paramagnetic specie, the $1/T$ dependance of χ' will compensate for the intrinsic sapphire thermal sensitivity. The mode frequency passes through a maximum at a temperature T_0 , which depends on the nature and concentration of the dopants. Our resonators are machined from HEMEX sapphire monocrystals provided by Crystal System Inc.²⁵ Such a crystal is grown with the heat exchanger method allowing the growth of large sapphire boule with the lowest defects and impurities concentration. Fig. 3 shows the turnover temperatures as a function of the whispering gallery mode frequency for a $2R = 50$ mm and $H = 20$ mm sapphire resonator.

All whispering gallery modes in a large frequency range present a turnover temperature almost independent of the mode order m . Luiten⁶ demonstrated that it is due to the predominance of the Mo^{3+} ion, whose ESR frequency is 165 GHz. The Mo^{3+} concentration was estimated to be of the order of some 0.1 ppm. The spread in turnover temperatures observed for low frequency modes ($\nu < 12$ GHz) could result from Cr^{3+} or/and Fe^{3+} residuals. The concentration of these residuals should be very low as the turnover temperature imposed by the Mo^{3+} ions is not greatly affected. Indeed, other measurements show that Cr^{3+} and Fe^{3+} concentrations are of some tens of ppb.^{2,26} Figure 4 shows the temperature dependance of the $WGH_{16,0,0}$ mode at 11.565 GHz of the same resonator and the theoretical predictions. Equation (5) evaluated with χ_0^{VV} and 0.15 ppm of Mo^{3+} represents well the experimental frequency variation shown in Figure 4.

IV. RESONATOR POWER SENSITIVITY

In the CSO, the sapphire whispering gallery mode resonator is simply inserted in the positive feedback loop of an electronic amplifier to form an oscillator as schematised in Figure 5. The CSO is completed by two servos to stabilize the power injected into the resonator and the phase lag along the sustaining loop.²⁷ The error signals needed for these two servos are derived from the low frequency voltages generated by two tunnel diodes placed near the resonator input port (see Figure 5). We build two identical oscillators: CSO-1 and CSO-2, a third unit being under construction. These

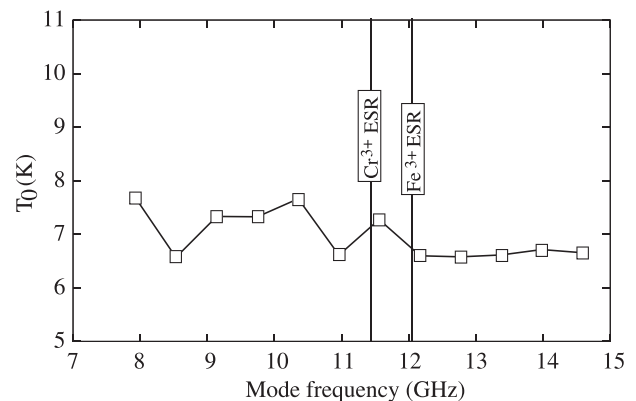


FIG. 3. $2R = 50$ mm, $H = 20$ mm HEMEX resonator: turnover temperature T_0 as a function of the mode frequency for $WGH_{m,0,0}$ modes with $4 \leq m \leq 21$.

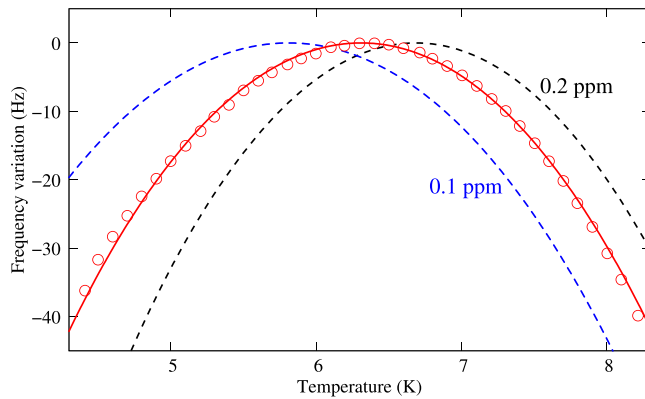


FIG. 4. $WGH_{16,0,0}$ mode frequency vs temperature variation for a 50 mm diameter and 20 mm high HEMEX sapphire resonator. Red open circles: experimental data. Dashed lines: Frequency calculated with the Van Vleck model with a Mo^{3+} ions concentration of 0.1 ppm (blue dashed line), 0.2 ppm (black dashed line), and 0.15 ppm (solid red line).

three instruments are intended to serve as references for ultra high resolution short term frequency stability measurements in the frame of the OSCILLATOR-IMP project.²⁸ The two CSOs are based on a $2R = 54$ mm and $H = 30$ mm HEMEX resonator designed to operate on the quasi-transverse magnetic whispering gallery mode $WGH_{15,0,0}$ near 10 GHz. For this resonator, the electromagnetic field is confined inside a volume $V_{eff} \approx 17$ cm³. The Table II gives the current resonators characteristics as measured with a network analyzer using a -10 dBm probe signal.

The Q-factor depends of the crystal quality but also of its cleanliness. It can be affected by spurious modes and by some geometrical imperfections in the cavity symmetry or in the coupling probes alignment. Generally, multiple cool-downs and fine step-by-step adjustments are required to get the highest unloaded Q-factor only limited by the sapphire

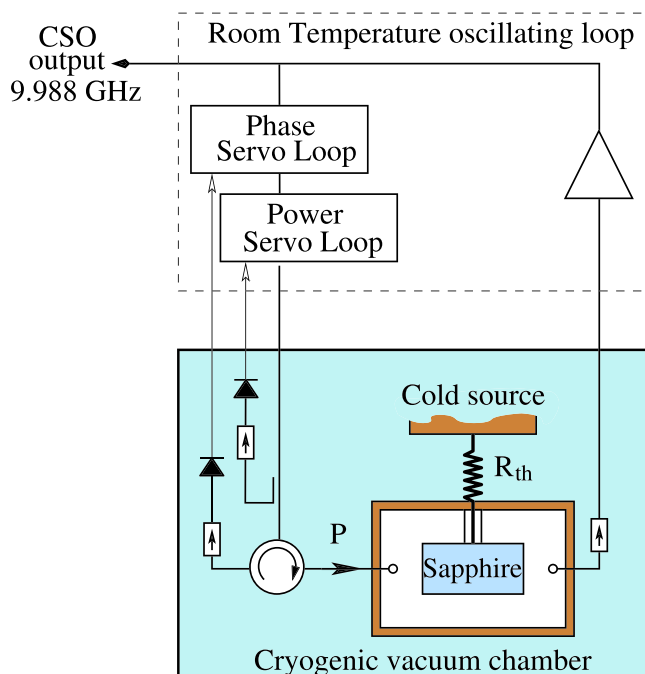


FIG. 5. Scheme of the Cryogenic sapphire oscillator. The cold source is a two-stages pulse-tube cryocooler.

TABLE II. The two resonators' parameters: T_0 : turnover temperature, Q_0 : unloaded Q-factor, β_1 and β_2 : coupling coefficient at the input and output ports respectively. P_0 : turnover power at which the resonator frequency is maximum. $\frac{\Delta\nu}{\Delta P}$ the frequency power sensitivity slope for $P \gg P_0$.

	T_0 (K)	Q_0	β_1	β_2	P_0 (μ W)	$\frac{\Delta\nu}{\Delta P}$ at high power (Hz/W)
CSO-1	6.23	2.0×10^9	1	0.1	120	-91
CSO-2	6.18	0.7×10^9	1	0.1	300	-39

dielectric losses. This was realized for CSO-1, still not for CSO-2 what explains its relative low Q-factor. For each resonator, the coupling coefficients have been set near their optimal value, i.e., $\beta_1 \approx 1$ and $\beta_2 \ll 1$. The injected power P is almost entirely dissipated into the resonator. When the resonator is stabilized at its turnover temperature, its thermal sensitivity nulls at first order, and the CSO frequency stability is no longer limited by the cold source temperature fluctuations. The current limitation in the frequency instability is not clearly established. The resonator power to frequency conversion constitutes one possible limitation²⁹ and needs, thus, to be investigated. To measure the CSO frequency sensitivity to the injected power, we follow the beatnote frequency changes when the power is varied in one CSO, while all other parameters being kept constant. Tunnel diodes placed at a low temperature turn out to be very sensitive and can be damaged if the incident power is too high. In the current resonator implementation, the maximal injected power has been limited to about 1 mW. Figure 6 shows the relative frequency variation as a function of the injected power for CSO-1 and CSO-2. The $WGH_{15,0,0}$ mode frequency passes through a maximum at a given power P_0 and exhibits for $P \gg P_0$ a linear negative sensitivity. The slopes at high power $\frac{\Delta\nu}{\Delta P}$ and P_0 , which depend on the resonator, are given in the Table II.

When the injected power P is increased, the resonator frequency will vary through different processes:

Thermal effect: The resonator is linked by a thermal resistance R_{th} to the cold source stabilized at the temperature T_S . The resonator temperature is $T = T_S + R_{th}P$. In the current

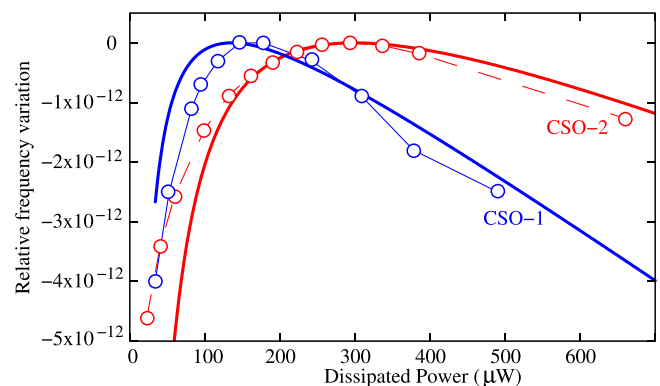


FIG. 6. Relative frequency variation vs dissipated power for CSO-1 (blue) and CSO-2 (red). The open circles are the experimental points. The solid bold lines are the theoretical expectations calculated from Eq. (10) assuming a concentration of 0.2 ppm of Mo^{3+} and 10 ppb of Cr^{3+} .

design, $R_{th} \approx 2 \text{ KW}^{-1}$. Thus for $P = 1 \text{ mW}$, the increase in the resonator temperature is only 2 mK, which, around the turnover temperature, induces a relative frequency shift less than 5×10^{-14} . This effect will give a negligible contribution in the experimentally accessible range of power.

Radiation pressure: The stress induced by the stored energy results in a resonator expansion and a decrease in the dielectric constant. The resulting resonator linear frequency to power sensitivity has been previously evaluated and can be written as^{29,30}

$$\frac{\Delta\nu}{\Delta P} = \kappa \frac{Q_0}{V_{eff}}, \quad (6)$$

with $\kappa \approx -7.2 \times 10^{-13} \text{ Pa}^{-1}$.

In the preceding works, the radiation pressure effect was assumed to be the major cause of the resonator power sensitivity. Indeed at a high power, this linear power dependence dominates the resonator frequency power sensibility. Equation (6) gives a sensitivity of -85 HzW^{-1} and -40 HzW^{-1} for CSO-1 and CSO-2 respectively, which are compatible with the experimental observations (see Table II).

ESR saturation: The third effect arises from the saturation of the ESR. To get an approximation of the RF magnetic field seen by the ions, we neglect its space variations. Over the effective volume V_{eff} , we take it as a constant and equals to its mean value \bar{B} defined as

$$\bar{B}^2 = \frac{1}{V_{eff}} \iiint BB^* dv. \quad (7)$$

The stored energy is proportionnal to the power dissipated inside the resonator

$$E_{stored} = \mu_0 \bar{B}^2 V_{eff} = \frac{Q_0 P}{2\pi\nu_0}. \quad (8)$$

The amplitude of the ac-magnetic field can be thus written as

$$\bar{B} = \sqrt{\frac{\mu_0 Q_0 P}{2\pi\nu_0 V_{eff}}}. \quad (9)$$

With the typical resonator parameters, i.e., $Q_0 = 10^9$, $P = 1 \text{ mW}$, $\nu_0 = 10 \text{ GHz}$, and $V_{eff} = 17 \text{ cm}^3$, we find $\bar{B} = 1 \text{ mT}$, which is about three orders of magnitude higher than the transverse magnetic field existing inside a 50Ω coaxial cable where a 1 mW microwave signal is propagating. For a signal frequency ν not too far from the ESR frequency, i.e., $|\nu - \nu_{mn}| \leq \text{few } \Delta\nu_{mn}$, the saturation of the ESR arises very rapidly when the injected power is increased. The ion energy level populations tend to balance themselves, and the induced magnetic susceptibility goes to zero. For a signal power higher than P_0 , only remains the linear power sensitivity imposed by the radiation pressure effect.

Equation (5) is now adapted to represent the resonator sensitivity to the injected power P

$$\frac{\nu(P) - \nu_0}{\nu_0} = A(T_S + R_{th}P)^4 + \frac{\kappa}{\nu_0} \frac{Q_0}{V_{eff}} P - \eta \frac{\chi'(\nu, P)}{2}. \quad (10)$$

This equation has been used to compute the relative frequency variation as a function of the dissipated power. The result is given in Figure 6 (bold lines) assuming a concentration of 0.2 ppm of Mo^{3+} and 10 ppb of Cr^{3+} for both resonators. We found about the same shape in the power dependences by replacing chromium by 1 ppb of Fe^{3+} . As previously mentioned, the model overestimates the saturation of the ESR for Fe^{3+} , whose concentration has been measured of the order of 10 ppb in similar sapphire crystals. It should also be pointed out that the value of P_0 is greatly dependant of the relaxation times τ_1 and τ_2 , which are not known with accuracy. Nevertheless, our model explains qualitatively well the power sensitivity of the sapphire resonator.

V. APPLICATION TO THE REALIZATION OF AN ULTRA STABLE OSCILLATOR

We can conclude from the previous observations (see Figure 6) that it exists for each resonator a value of the injected power, i.e., P_0 for which the sensitivity to the power fluctuations nulls to the first order. At that point, the CSO frequency stability would not any more be limited by the fluctuations of the injected power. To verify this assumption, we conducted the following measurement: CSO-2 was operated in a degraded mode with its power servo in open loop. A laboratory DC-power supply was used to bias the voltage controlled attenuator (VCA) placed in the oscillator loop and that controls the level of the injected power. The DC voltage V generated by the power supply fluctuates with time following a random walk process. We observed that its standard deviation $\sigma_V(\tau)$ when averaged over $\tau = 1 \text{ s}$ is of the order of $10 \mu\text{V}$. At longer integration time, i.e., $\tau \geq 10 \text{ s}$, $\sigma_V(\tau)$ is degraded proportionally to $\tau^{1/2}$, typical of a random walk process. Through the VCA, the power injected in the resonator, and, thus, the CSO frequencies are modulated by this voltage noise. Figure 7 shows the relative frequency stability (Allan standard deviation) measured by beating the two CSOs for different values of the power injected in CSO-2 imposed by the DC-voltage V . CSO-1 was nominally running with its power servo on.

When the injected power is tuned to $P_0 = 300 \mu\text{W}$, the gain of the phase servo is optimal, and the measured short term frequency stability at $\tau = 1 \text{ s}$ is 1.5×10^{-15} , which

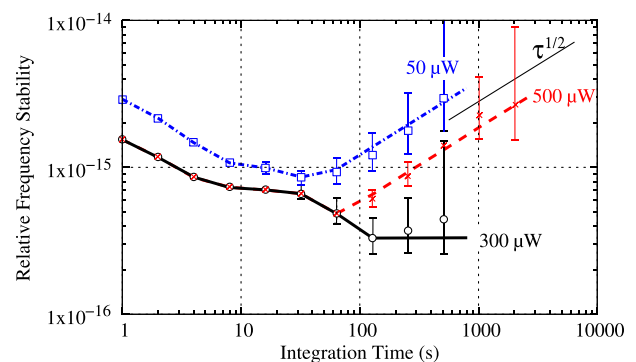


FIG. 7. Measured frequency stability (Allan standard deviation) for different values of the power injected in CSO-2. CSO-2 operated in a degraded mode without power control.

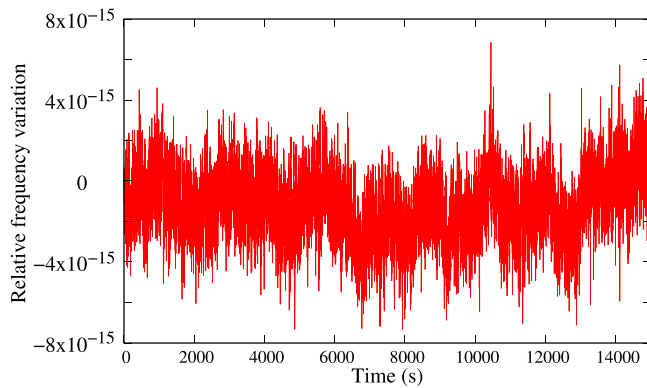


FIG. 8. Relative frequency variation during a period of about 4 h measured by beating two almost identical optimized CSOs.

includes the contributions of both CSOs. At this level of power, the CSO frequency stability would not be limited by the fluctuations of the injected power. Indeed, the relative frequency stability improves as τ is increased to reach a flicker floor of 3×10^{-16} . At a high power, i.e., $P = 500 \mu\text{W}$, the short frequency stability remains unaltered. Then, for $\tau \geq 100$ s, the frequency stability is clearly limited by random walk process. The measured frequency noise level is compatible with the DC-voltage noise and the resonator sensitivity at such a high injected power. At low injected power, $P = 50 \mu\text{W}$, the short term frequency stability for $\tau \leq 10$ s is degraded as the gain of the phase servo, which is proportional to P , is decreased. At longer integration time $\tau \geq 100$ s, the measured frequency stability is degraded proportionally to $\tau^{1/2}$ with a frequency noise level higher than for $P = 500 \mu\text{W}$ as the power sensitivity at low injected power is higher.

Eventually, in both oscillators, the resonator temperature and the injected power were stabilized at their inversion point, i.e., T_0 and P_0 respectively. The relative frequency stability is measured by beating the signals of the two identical CSOs, separated by 7.029 MHz, with a frequency counter without dead time. Figure 8 shows the raw data recorded for a quiet period of 4 h.

The relative frequency stability (Allan standard deviation) of one CSO is presented in Figure 9: 3 dB was subtracted considering that the total measured noise is the sum of the contribution of two identical oscillators.

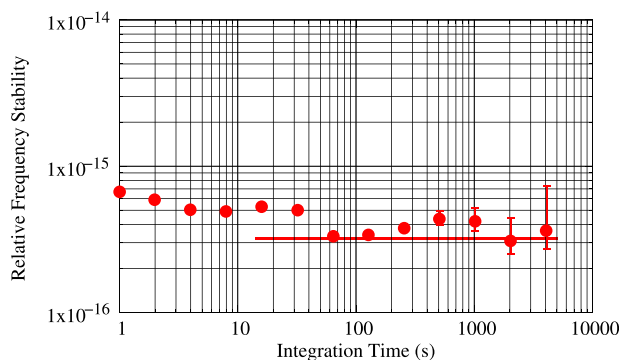


FIG. 9. Relative frequency stability of one optimized CSO. The Allan deviation has been calculated from the raw data of Figure 8, and thanks to the freeware SigmaTheta³¹ available on Ref. 32.

For $1 \text{ s} \leq \tau \leq 10\,000 \text{ s}$ the relative frequency stability is better than 7×10^{-16} . A flicker floor of 3×10^{-16} is reached at 100 s. The first small hump appearing around $\tau = 30$ s could be due to a residual pumping we have detected in the temperature servo of one resonator. The second hump around $\tau = 800$ s comes from the pumping of the laboratory climatisation. This second hump could be due to the frequency stability measurement instrument sensitivity to the room temperature.

VI. CONCLUSION

In summary, we exploited the Van Vleck model to describe the saturation of the electron spin resonance of the paramagnetic species contained in a high quality sapphire resonator. The proposed model explains qualitatively well the frequency-to-power sensitivity of the sapphire resonator. The ESR saturation and the sapphire intrinsic sensitivity compensate themselves at a given injected power, leading to a turnover in the frequency-vs-power curve. It is thus demonstrated that the CSO stabilized at this power value presents an exceptional short term frequency stability better than 7×10^{-16} for $\tau \leq 10\,000$ s.

ACKNOWLEDGMENTS

The work has been realized in the frame of the ANR projects: Equipex Oscillator-Imp and Emergence ULISS-2 G. The authors would like to thank the Council of the Région de Franche-Comté for its support to the Projets d'Investissements d'Avenir and the FEDER for funding one CSO.

- ¹B. C. Barish, G. Billingsley, J. Camp, W. P. Kells, G. H. Sanders, S. E. Whitcomb, L. Y. Zhang, R.-Y. Zhu, P. Z. Deng, J. Xu, G. Q. Zhou, and Y. Z. Zhou, *IEEE Trans. Nucl. Sci.* **49**, 1233 (2002).
- ²K. Benmessai, W. G. Farr, D. L. Creedon, Y. Reshitnyk, J.-M. Le Floch, T. Duty, and M. E. Tobar, *Phys. Rev. B* **87**, 094412 (2013).
- ³S. Grop, W. Schäfer, P.-Y. Bourgeois, Y. Kersalé, M. Oxborrow, E. Rubiola, and V. Giordano, *IEEE Trans. Ultrason., Ferroelectr., Freq. Control* **58**, 1694–1697 (2011).
- ⁴V. Giordano, S. Grop, B. Dubois, P.-Y. Bourgeois, Y. Kersalé, E. Rubiola, G. Haye, V. Dolgovskiy, N. Bucalovicy, G. D. Domenico, S. Schilt, J. Chauvin, and D. Valat, *Rev. Sci. Instrum.* **83**, 085113 (2012).
- ⁵A. Mann, A. Giles, D. Blair, and M. Buckingham, *J. Phys. D: Appl. Phys.* **25**, 1105 (1992).
- ⁶A. N. Luiten, A. Mann, and D. Blair, *J. Phys. D: Appl. Phys.* **29**, 2082 (1996).
- ⁷P. Bourgeois, N. Bazin, Y. Kersalé, V. Giordano, M. Tobar, and M. Oxborrow, *Appl. Phys. Lett.* **87**, 224104 (2005).
- ⁸K. Benmessai, D. L. Creedon, M. E. Tobar, P. Y. Bourgeois, Y. Kersalé, and V. Giordano, *Phys. Rev. Lett.* **100**, 233901 (2008).
- ⁹D. L. Creedon, K. Benmessai, W. P. Bowen, and M. E. Tobar, *Phys. Rev. Lett.* **108**, 093902 (2012).
- ¹⁰D. L. Creedon, K. Benmessai, and M. E. Tobar, *Phys. Rev. Lett.* **109**, 143902 (2012).
- ¹¹W. G. Farr, D. L. Creedon, M. Goryachev, K. Benmessai, and M. E. Tobar, *Phys. Rev. B* **88**, 224426 (2013).
- ¹²A. E. Siegman, *Microwave Solid-state Maser* (McGraw-Hill, New York, 1964).
- ¹³J. Vanier and C. Audoin, *The Quantum Physics of Atomic Frequency Standards* (Adam Hilger, Bristol, UK, 1989), Vol. 1.
- ¹⁴K. H. J. Buschow and F. R. de Boer, *Physics of Magnetism and Magnetic Materials* (Kluwer academic publishers, New York, 2003).
- ¹⁵N. Majlis, *Quantum Theory of Magnetism* (World Scientific Publishing, 2007).
- ¹⁶K. J. Standley and R. A. Vaughan, *Phys. Rev.* **139**, A1275 (1965).
- ¹⁷E. G. Sharoyan, O. S. Torosyan, E. A. Markosyan, and V. T. Gabrielyan, *Phys. Status Solidi B* **65**, 773–778 (1974).

- ¹⁸K. N. Kocharyan, A. A. Mirzakhanyan, and E. G. Sharoyan, *Physica Status Solidi B* **94**, K129 (1979).
- ¹⁹G. S. Bogle and H. F. Symmons, *Proc. Phys. Soc.* **73**, 531 (1959).
- ²⁰J. H. V. Vleck, *Science* **201**, 113 (1978).
- ²¹R. Boča, *Coord. Chem. Rev.* **248**, 757 (2004).
- ²²V. Branginsky, V. S. Ilchenko, and K. Bagdassarov, *Phys. Lett. A* **120**, 300 (1987).
- ²³P. Bourgeois and V. Giordano, *IEEE Trans. Microwave Theory Tech.* **53**, 3185 (2005).
- ²⁴D. Cros and P. Guillon, *IEEE Trans. Microwave Theory Tech.* **38**, 1667 (1990).
- ²⁵F. Schmid and D. Viechnicki, *Solid State Tech.* **16**(9), 45–48 (1973).
- ²⁶R. Kovacich, A. Mann, and D. Blair, *J. Phys. D: Appl. Phys.* **30**, 3146 (1997).
- ²⁷S. Grop, P.-Y. Bourgeois, N. Bazin, Y. Kersalé, E. Rubiola, C. Langham, M. Oxborrow, D. Clapton, S. Walker, J. D. Vicente, and V. Giordano, *Rev. Sci. Instrum.* **81**, 025102 (2010).
- ²⁸See <http://www.oscillator-imp.com/> for details on the OSCILLATOR-IMP Project.
- ²⁹N. R. Nand, S. R. Parker, E. N. Ivanov, J.-M. Le Floch, J. G. Hartnett, and M. E. Tobar, *Appl. Phys. Lett.* **103**, 043502 (2013).
- ³⁰S. Chang, A. G. Mann, A. N. Luiten, and D. G. Blair, *Phys. Rev. Lett.* **79**, 2141 (1997).
- ³¹F. Vernotte and E. Lantz, *IEEE Trans. Ultrason., Ferroelectr., Freq. Control* **59**, 523 (2012).
- ³²See <http://theta.obs-besancon.fr/spip.php?article103&lang=fr> for the free software download.